

Adaptive 3D finite elements with high aspect ratio for dendritic growth of a binary alloy including fluid flow induced by shrinkage

Jacek Narski^{1,2} and Marco Picasso¹

(Communicated by John Lowengrub and Mark Sussman)

Abstract: An adaptive phase field model for the solidification of binary alloys in three space dimensions is presented. The fluid flow in the liquid due to different liquid/solid densities is taken into account. The unknowns are the phase field, the alloy concentration and the velocity/pressure in the liquid. Continuous, piecewise linear finite elements are used for the space discretization, a semi-implicit scheme is used for time discretization. An adaptive method allows the number of degrees of freedom to be reduced, the mesh tetrahedrons having high aspect ratio whenever needed. Numerical results show that our method is effective and allows to perform complicated simulations with relatively few computer resources needed. The simultaneous evolution of several solutal dendrites can be efficiently simulated on a single workstation.

Keyword: mesh adaptation, solidification, phase-field, Navier-Stokes, finite elements

1 Introduction

In recent years, considerable progress has been made in numerical simulation of solidification processes at microscopic scale [Boettinger, Coriell, Greer, Karma, Kurz, Rappaz, and Trivedi (2000)]. Although sharp interface [Juric and Tryggvason (1996); Jacot and Rappaz (2002)] and level-set models [Fried (2004); Gibou, Fedkiw, Caffisch, and Osher (2003)] have proved to be efficient, the phase field method emerged as a method of choice in order to simulate dendritic growth in binary alloys [Collins and Levine

(1985); Caginalp and Xie (1993); Kobayashi (1993); Karma (1994); Warren and Boettinger (1995); Chen (2002); Echebarria, Folch, Karma, and Plapp (2004)]. In phase field models, the location of the solid and liquid phases in the computational domain is described by introducing an order parameter, the phase field, which varies smoothly from one in the solid to zero in the liquid through a slightly diffused interface. The main difficulty when solving numerically phase field models is due to the very rapid change of the phase field (and also of the concentration field in alloys) across the diffuse interface, whose thickness has to be taken very small (between 1 and 10 nm) to correctly capture the physics of the phase transformation. A high spatial resolution is therefore needed to describe the smooth transition. In order to reduce the computational time and the number of grid points adaptive isotropic finite elements [Schmidt (1996); Provatas, Goldenfeld, and Dantzig (1999)] have been used. Further reduction of the number of nodes has been achieved using adaptive finite elements with high aspect ratio [Burman and Picasso (2003); Burman, Jacot, and Picasso (2004)].

The influence of inter-dendritic liquid flow has already been taken into account in dendritic simulations [Ni and Beckermann (1991); Beckermann, Diepers, Steinbach, Karma, and Tong (1999); Nestler, Wheeler, Ratke, and Stöcker (2000); Jeong, Goldenfeld, and Dantzig (2001); Boettinger, Warren, Beckermann, and Karma (2002); Tönhardt and Amberg (2000); Hong, Zhu, and Lee (2006)]. Also, the inter-dendritic liquid flow induced by shrinkage — that is to say the flow induced by the fact that solid and liquid densities are different — has been considered [Anderson,

¹ Institut d'Analyse et Calcul Scientifique, Ecole Polytechnique Fédérale de Lausanne, 1015 Lausanne, Switzerland

² Supported by the Swiss National Science Foundation

McFadden, and Wheeler (2000, 2001); Heinrich and Poirier (2004); Griebel, Merz, and Neunhoffer (1999); Sun and Beckermann (2004); Conti (2001, 2004)].

The goal of this paper is to take into account the inter-dendritic liquid flow due to shrinkage, using adaptive finite elements with high aspect ratio as in [Narski and Picasso (2006)] but in three space dimensions. It will be shown that the use of 3D adaptive finite elements with high aspect ratio allows complex dendritic simulations to be performed on standard workstations.

The outline of the paper is following. In the following section, we present the model. The numerical method is described in section 3. In section 4, we study the influence of shrinkage on dendritic growth.

2 The model

The solidification of an alloy at mesoscopic scale depends on temperature and concentration. The former is assumed to be a known parameter, the latter is altered by convection in the melt. Thus the model consists of a coupled set of equations for the phase field, concentration, velocity and pressure.

The equations are derived using a volume averaging technique in the similar way as in [Ni and Beckermann (1991); Beckermann, Diepers, Steinbach, Karma, and Tong (1999)]. The key idea is to develop two sets of equations (for solid and liquid phases) and transform them into one set using averaging over small volume and introducing average quantities.

In the following we present the averaged mass, momentum and species conservation equation for binary alloy undergoing a solid/liquid phase transition. As in [Anderson, McFadden, and Wheeler (2000, 2001); Heinrich and Poirier (2004); Griebel, Merz, and Neunhoffer (1999); Sun and Beckermann (2004)], we take into account the fact that the solid and liquid densities are different. Details of the derivation can be found in [Narski and Picasso (2006)].

2.1 Mass conservation

The solidification of a binary alloy in a bounded domain Ω of \mathbb{R}^3 between time 0 and t_{end} is considered. Let $\phi : \Omega \times (0, t_{end}) \rightarrow \mathbb{R}$ be the phase field describing presence of solid ($\phi = 1$) or liquid ($\phi = 0$). The phase field ϕ varies smoothly but rapidly from zero to one in a thin region of width δ , the so-called solid/liquid diffused interface. Let ρ_s and ρ_l be the constant solid and liquid densities (for most alloys $\rho_l < \rho_s$). Then the average density $\rho : \Omega \times (0, t_{end}) \rightarrow \mathbb{R}$ is defined by

$$\rho = \rho_s \phi + \rho_l (1 - \phi).$$

Let $\mathbf{v}_s, \mathbf{v}_l$ be the solid and liquid velocities, respectively. In this model, the solid velocity \mathbf{v}_s is a known constant (in most cases $\mathbf{v}_s = \mathbf{0}$), whereas \mathbf{v}_l is unknown. Then, the average velocity $\mathbf{v} : \Omega \times (0, t_{end}) \rightarrow \mathbb{R}^3$ is defined by

$$\rho \mathbf{v} = \rho_s \phi \mathbf{v}_s + \rho_l (1 - \phi) \mathbf{v}_l.$$

Averaging the mass conservation equation in the solid and liquid regions yields

$$\frac{\partial \rho}{\partial t} + \text{div}(\rho \mathbf{v}) = 0. \quad (1)$$

An equivalent formulation is:

$$\text{div} \mathbf{v} = -\frac{\rho_s - \rho_l}{\rho} \left(\frac{\partial \phi}{\partial t} + (\mathbf{v} \cdot \nabla) \phi \right),$$

thus the solidification shrinkage is a source of mass in the liquid.

It should be noted that, in the sharp interface limit (that is to say when the width of the solid-liquid interface δ tends to zero), then the phase field ϕ is the characteristic function of the solid so that the density ρ becomes a step function and (1) has to be understood in the sense of distributions. Then, the following relation holds on the solid/liquid interface:

$$[\rho]V + [\rho \mathbf{v} \cdot \mathbf{n}] = 0,$$

where $[\cdot]$ denotes the jump of the inside quantity across the interface, V is the normal velocity of the solid/liquid interface and the vector \mathbf{n} denotes the normal to the interface. For instance, when

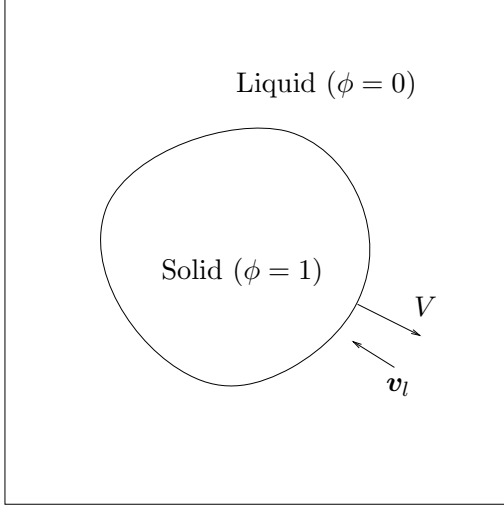


Figure 1: Solidification of a solid seed with density ρ_s larger than the liquid density ρ_l : as the solid/liquid interface moves with normal velocity V toward the boundary of the calculation domain Ω , liquid flows with velocity \mathbf{v}_l toward the solid.

solid is not moving ($\mathbf{v}_s = 0$), this condition reduces to

$$\mathbf{v}_l \cdot \mathbf{n} = \frac{\rho_s - \rho_l}{\rho_l} V,$$

see Figure 1.

2.2 Momentum conservation

The momentum equation writes, in the whole computational domain $\Omega \times (0, t_{end})$:

$$\begin{aligned} & \rho \frac{\partial \mathbf{v}}{\partial t} + \rho (\mathbf{v} \cdot \nabla) \mathbf{v} \\ & + \operatorname{div} \left(\rho \frac{\phi \rho_s}{(1 - \phi) \rho_l} (\mathbf{v} - \mathbf{v}_s) \otimes (\mathbf{v} - \mathbf{v}_s) \right) \\ & - 2 \operatorname{div} \left(\mu_l \boldsymbol{\varepsilon}(\mathbf{v}) \right) + \nabla p + \frac{1}{\varepsilon} \phi^2 (\mathbf{v} - \mathbf{v}_s) = 0, \quad (2) \end{aligned}$$

where p is pressure, μ_l the liquid viscosity and $\boldsymbol{\varepsilon}(\mathbf{v}) = 1/2(\nabla \mathbf{v} + \nabla \mathbf{v}^T)$ the rate of deformation tensor of the average velocity \mathbf{v} . The penalty term

$$\frac{1}{\varepsilon} \phi^2 (\mathbf{v} - \mathbf{v}_s)$$

with a penalty parameter $\varepsilon \ll 1$ is added to the momentum equation in order to force the average

velocity field \mathbf{v} to equal the solid velocity \mathbf{v}_s in the solid region ($\phi = 1$). This term is consistent with the method proposed in [Beckermann, Diepers, Steinbach, Karma, and Tong (1999)], where the interfacial stress term is modelled and the resulting additional term is proportional to $\frac{\phi^2}{\delta^2} \mathbf{v}$.

It should be stressed that in the liquid far from the solid/liquid interface ($\phi = 0$), the mass and momentum equations (1) (2) reduce to the incompressible Navier-Stokes equations whereas in the solid region ($\phi = 1$), due to the penalty term, the velocity equals the solid velocity \mathbf{v}_s as ε becomes small.

The validity of this equation is restricted to cases where no closed liquid regions are present and the solidification shrinkage can be compensated by a liquid inflow through the boundary. When closed liquid regions are created during the solidification process the shrinkage causes formation of a micropores. This physical phenomenon requires a new model of a phase field where three phases can coexist together — solid, liquid and gas, this being not included in our model. Therefore, the numerical simulation should be stopped whenever closed liquid regions are present in the solid. The other criterion of the microporosity formation is the pressure drop in the melt exceeding certain critical value — our model is therefore capable of indicating the regions where microporosity may appear.

2.3 Species conservation

The averaged concentration conservation equation writes

$$\begin{aligned} & \frac{\partial c}{\partial t} + \operatorname{div} \left(\frac{c}{k \rho_s \phi + \rho_l (1 - \phi)} (\rho \mathbf{v} + (k - 1) \rho_s \phi \mathbf{v}_s) \right) \\ & - \operatorname{div} (D(\phi) \nabla c + \tilde{D}(c, \phi) \nabla \phi) = 0, \quad (3) \end{aligned}$$

where c is the average volumic concentration of the alloy, the partition coefficient k is obtained from the equilibrium phase diagram and

$$D(\phi) = \frac{k \rho_s \phi D_s + \rho_l (1 - \phi) D_l}{k \rho_s \phi + \rho_l (1 - \phi)}$$

is the averaged diffusion coefficient with D_s , D_l being the constant solid and liquid diffusion coef-

ficients. Finally,

$$\tilde{D}(c, \phi) = D(\phi) \frac{c(\rho_l - k\rho_s)}{k\rho_s\phi + \rho_l(1 - \phi)}.$$

2.4 Phase-field

We consider a standard phase-field equation for the solid phase moving with constant velocity \mathbf{v}_s :

$$\begin{aligned} \frac{1}{\mu_k} \left(\frac{\partial \phi}{\partial t} + \mathbf{v}_s \cdot \nabla \phi \right) = \\ \Gamma \left(\operatorname{div}(A(\nabla \phi) \nabla \phi) - \frac{\phi(1 - \phi)(1 - 2\phi)}{\delta^2} \right) \\ + \left(T_m + m_l \frac{c}{k\rho_s\phi + \rho_l(1 - \phi)} - T \right) \frac{\phi(1 - \phi)}{\delta}. \end{aligned} \quad (4)$$

Here μ_k denotes the kinetic mobility, Γ is the Gibbs-Thomson coefficient. The term $\operatorname{div}A(\nabla \phi) \nabla \phi$ is the functional derivative (that is to say the Frechet derivative) of the surface energy

$$\frac{1}{2} \int_{\Omega} a(\nabla \phi(\mathbf{x}))^2 |\nabla \phi(\mathbf{x})|^2 d\mathbf{x},$$

where a is the real-valued function defined by

$$a(\xi) = (1 - \bar{a}) \left(1 + \frac{4\bar{a}}{1 - 3\bar{a}} \frac{\xi_x^4 + \xi_y^4 + \xi_z^4}{\|\xi\|^4} \right)$$

with \bar{a} the anisotropy parameter and the vector $\xi = \{\xi_x, \xi_y, \xi_z\} \in \mathbb{R}^3 \setminus \{0\}$. The term $\phi(1 - \phi)(1 - 2\phi)$ in (4) is the derivative of the double well which forces the phase field to values close to zero or one. Finally, the last term in (4) is a source term accounting for the energy due to the solid-liquid phase transformation, T_m is the melting temperature of the pure substance, m_l is the slope of the liquidus line in the equilibrium phase diagram. The temperature $T < T_m$ is a given quantity in this model.

2.5 Summary of the model

The goal of the present model is to find the phase field $\phi : \Omega \times (0, t_{end}) \rightarrow \mathbb{R}$, the volumic concentration $c : \Omega \times (0, t_{end}) \rightarrow \mathbb{R}$, the velocity $\mathbf{v} : \Omega \times (0, t_{end}) \rightarrow \mathbb{R}^3$ and the pressure $p : \Omega \times (0, t_{end}) \rightarrow$

\mathbb{R} , satisfying equations (4), (3), (2) and (1). Natural boundary conditions apply on the boundary of the calculation domain Ω for ϕ , c and \mathbf{v} . Moreover, initial conditions at time $t = 0$ must be prescribed for ϕ , c and \mathbf{v} .

Existence and uniqueness of solutions for this model in the absence of liquid flow and for sufficiently small \bar{a} (small anisotropy) are proved in [Burman and Rappaz (2003)]. *A posteriori* error estimation and adaptive finite elements are presented in [Burman and Picasso (2003)]. Existence and convergence of solutions in presence of liquid flow is an open problem. Numerical results in presence of liquid flow and in two space dimensions has been presented in [Narski and Picasso (2006)]. Our goal is to extend the model to 3D.

3 Numerical method

Equations (4) and (3) are discretized in time using an order one semi-implicit scheme. Equations (2) and (1) are solved using a splitting scheme. Space discretization is based on continuous, piecewise linear finite elements on tetrahedral adapted meshes. In order to reduce the number of degrees of freedom, the tetrahedrons may have large aspect ratio whenever needed. The refinement/coarsening criterion is based on an anisotropic error indicator. This error indicator is based on a *a posteriori* error estimator derived for simpler problems, namely elliptic problems [Picasso (2003b)], parabolic problems [Picasso (2003a)], Stokes problem [Picasso (2005a)], dendritic growth [Burman and Picasso (2003)]. See also [Burman, Jacot, and Picasso (2004)] for numerical simulations of coalescence in two space dimensions.

3.1 Discretization of the phase and concentration equations

Let τ be the time step, $t^n = n\tau$, $n = 0, 1, 2, \dots$. At each time step, given finite element approximations ϕ^{n-1} , c^{n-1} , \mathbf{v}^{n-1} , p^{n-1} of the phase, concentration, velocity and pressure at time t^{n-1} , we are first seeking for the phase ϕ^n such that

$$\begin{aligned}
& \int_{\Omega} \left(\frac{\phi^n - \phi^{n-1}}{\mu_k \tau} \boldsymbol{\psi} + (\mathbf{v}_s \cdot \nabla \phi^n) \boldsymbol{\psi} \right) \\
&= -\Gamma \int_{\Omega} \left(A(\nabla \phi^{n-1}) \nabla \phi^n \cdot \nabla \boldsymbol{\psi} \right. \\
&\quad \left. + \frac{S'(\phi^{n-1})(\phi^n - \phi^{n-1}) + S(\phi^{n-1})}{\delta^2} \boldsymbol{\psi} \right) \\
&+ \int_{\Omega} \left(T_m + m_l \frac{c^{n-1}}{k \rho_s \phi^{n-1} + \rho_l (1 - \phi^{n-1})} - T \right) \\
&\quad \times \frac{\phi^{n-1} (1 - \phi^{n-1})}{\delta} \boldsymbol{\psi},
\end{aligned}$$

for all test function $\boldsymbol{\psi}$ in the finite element space, where we have set $S(\phi) = \phi(1 - \phi)(1 - 2\phi)$. The above weak formulation leads to an invertible matrix whenever

$$\tau \leq C\delta^2, \quad (5)$$

where C depends only on μ_k , \bar{a} and Γ . Then, we are looking for c^n such that

$$\begin{aligned}
& \int_{\Omega} \frac{c^n - c^{n-1}}{\tau} \boldsymbol{\psi} + \int_{\Omega} D(\phi^n) \nabla c^n \cdot \nabla \boldsymbol{\psi} \\
& - \int_{\Omega} \frac{c^n}{k \rho_s \phi^n + \rho_l (1 - \phi^n)} (\rho \mathbf{v}^{n-1} + (k-1) \rho_s \phi^n \mathbf{v}_s) \cdot \nabla \boldsymbol{\psi} \\
& = - \int_{\Omega} \tilde{D}(c^{n-1}, \phi^n) \nabla \phi^n \cdot \nabla \boldsymbol{\psi}, \quad (6)
\end{aligned}$$

for all test function $\boldsymbol{\psi}$ in the finite element space.

3.2 Discretization of the fluid flow equations

Finally, we apply the standard Chorin-Temam non-incremental splitting scheme to find the velocity \mathbf{v}^n and pressure p^n , see for instance [Picasso and Rappaz (2001)] for a description in the framework of stabilized finite elements. This method allows velocity and pressure computations to be decoupled thus reducing the memory requirements. The algorithm consists of three steps.

1. First, we are seeking the predicted velocity $\mathbf{v}^{n-1/2}$ such that

$$\begin{aligned}
& \int_{\Omega} \left(\rho^n \frac{\mathbf{v}^{n-1/2} - \mathbf{v}^{n-1}}{\tau} + \rho^n (\mathbf{v}^{n-1} \cdot \nabla) \mathbf{v}^{n-1/2} \right) \cdot \mathbf{w} \\
& - \int_{\Omega} \rho^n \frac{\phi^n \rho_s}{(1 - \phi^n) \rho_l} (\mathbf{v}^{n-1} - \mathbf{v}_s) \otimes (\mathbf{v}^{n-1/2} - \mathbf{v}_s) : \boldsymbol{\varepsilon}(\mathbf{w}) \\
& + \int_{\Omega} \mu_l \boldsymbol{\varepsilon}(\mathbf{v}^{n-1/2}) : \boldsymbol{\varepsilon}(\mathbf{w}) = 0,
\end{aligned}$$

is satisfied for all test functions \mathbf{w} , where we have set $\rho^n = \rho_s \phi^n + \rho_l (1 - \phi^n)$. The predicted velocity obviously does not satisfy the mass conservation equation (1).

2. In the second step, given $\mathbf{v}^{n-1/2}$ we find the pressure p^n such that

$$\begin{aligned}
& \int_{\Omega} \operatorname{div} (\rho^n \mathbf{v}^{n-1/2}) q + \int_{\Omega} \frac{\rho^n - \rho^{n-1}}{\tau} q \\
& + \sum_{\text{tetr. } K} \max \left\{ \frac{\alpha h_K^2}{\mu_l}, \frac{\tau}{\rho^n} \right\} \int_K \rho^n \nabla p^n \cdot \nabla q = 0,
\end{aligned}$$

for all test function q . The coefficient $\alpha > 0$ is a dimensionless stabilisation parameter (we have chosen $\alpha = 0.01$ in our simulations), h_K denotes the characteristic size of a tetrahedron K . When the tetrahedron is highly stretched, h_K should be the size in the minimum stretching direction, $\lambda_{3,K}$ according to the notations of the next subsection, see [Micheletti, Perotto, and Picasso (2003)] for a theoretical justification for the Stokes problem.

3. Finally, we are seeking for the corrected velocity \mathbf{v}^n such that

$$\begin{aligned}
& \int_{\Omega} \left(\rho^n \frac{\mathbf{v}^n - \mathbf{v}^{n-1/2}}{\tau} \right) \cdot \mathbf{w} + \int_{\Omega} \frac{(\phi^n)^2}{\varepsilon} (\mathbf{v}^n - \mathbf{v}_s) \cdot \mathbf{w} \\
& - \int_{\Omega} p^n \operatorname{div} \mathbf{w} = 0
\end{aligned}$$

for all test functions \mathbf{w} .

3.3 Adaptive finite elements with large aspect ratio

To simulate reliably the interface the mesh size must be smaller than the interface width δ . With the typical values of δ of the order of $10^{-6}m$ and the computational domain Ω of size $10^{-3}m$ this would yield the number of mesh points to be bigger than 10^9 for a uniform grid. Thus the simulations of 3D dendritic growth would be intractable.

The important characteristic of the solidification problems is that all fields (phase, concentration, velocity) vary rapidly in the vicinity of the interface, while changing more slowly in the remaining regions. This suggests that a high grid resolution is necessary only in a small region of the

computational domain and one can hope that the use of anisotropic adaptive methods would drastically reduce the number of nodes. Indeed, in our simulations the meshes obtained have less than $3 \cdot 10^5$ nodes thus making the simulations possible even on the simple workstations. The average aspect ratio was as high as 100. For the same error tolerance isotropic adaptive meshes would require at least 100 times more vertices.

We now describe our adaptive finite element algorithm, the time step τ being kept constant and such that (5) holds. Let N be the number of time steps. The goal of the adaptive algorithm is to build successive tetrahedral meshes with large aspect ratio such that the relative estimated error of the concentration c in the $L^2(0, t_{end}; H^1(\Omega))$ norm is close to a preset tolerance TOL . For this purpose, we introduce an error indicator which requires some further notations. This error indicator measures the error of the concentration c in the directions of maximum and minimum stretching of the tetrahedron. The goal of the adaptive algorithm is then to equidistribute the error indicator in the directions of maximum and minimum stretching, and to align the directions of maximum and minimum stretching with the directions of maximum and minimum error. We refer to [Picasso (2003b,a); Burman and Picasso (2003)] for theoretical justifications for the two dimensional case.

The reason why the mesh adaptation algorithm is based on only on the error indicator for the concentration field is following. During numerical simulations of solidification c , ϕ and \mathbf{v} varies strongly in the small region corresponding to solid-liquid interface. We have chosen the concentration field to monitor mesh adaptation since it varies also in other regions.

We now describe in more details our error indicator. Its derivation is based on the anisotropic interpolation estimates derived in [Formaggia and Perotto (2001, 2003)]. Similar results have also been independently in [Kunert (2000)]. We refer to [Randrianarivony (2004); Creusé and Nicaise (2006); Formaggia, Micheletti, and Perotto (2004); Picasso (2005b)] for anisotropic a posteriori error estimates in the framework of

Stokes problem.

For any tetrahedron K of the mesh, let $T_K : \hat{K} \rightarrow K$ be the affine transformation which maps the reference tetrahedron \hat{K} into K . Let M_K be the Jacobian of T_K that is

$$\mathbf{x} = T_K(\hat{\mathbf{x}}) = M_K \hat{\mathbf{x}} + \mathbf{t}_K.$$

Since M_K is invertible, it admits a singular value decomposition $M_K = R_K^T \Lambda_K P_K$, where R_K and P_K are orthogonal and where Λ_K is diagonal with positive entries. In the following we set

$$\Lambda_K = \begin{pmatrix} \lambda_{1,K} & 0 & 0 \\ 0 & \lambda_{2,K} & 0 \\ 0 & 0 & \lambda_{3,K} \end{pmatrix} \text{ and } R_K = \begin{pmatrix} \mathbf{r}_{1,K}^T \\ \mathbf{r}_{2,K}^T \\ \mathbf{r}_{3,K}^T \end{pmatrix},$$

with the choice $\lambda_{1,K} \geq \lambda_{2,K} \geq \lambda_{3,K}$. A simple example of such a transformation is $x_1 = h_1 \hat{x}_1$, $x_2 = h_2 \hat{x}_2$, $x_3 = h_3 \hat{x}_3$, with $h_1 \geq h_2 \geq h_3$, thus

$$M_K = \begin{pmatrix} h_1 & 0 & 0 \\ 0 & h_2 & 0 \\ 0 & 0 & h_3 \end{pmatrix}$$

$$\lambda_{1,K} = h_1, \quad \lambda_{2,K} = h_2, \quad \lambda_{3,K} = h_3,$$

$$\mathbf{r}_{1,K} = \begin{pmatrix} 1 \\ 0 \\ 0 \end{pmatrix}, \quad \mathbf{r}_{2,K} = \begin{pmatrix} 0 \\ 1 \\ 0 \end{pmatrix}, \quad \mathbf{r}_{3,K} = \begin{pmatrix} 0 \\ 0 \\ 1 \end{pmatrix},$$

see Figure 2. In other words $\mathbf{r}_{1,K}$, $\mathbf{r}_{2,K}$ and $\mathbf{r}_{3,K}$ are the directions of the stretching ($\mathbf{r}_{1,K}$ being the direction of maximal stretching and $\mathbf{r}_{3,K}$ the direction of minimal stretching), while $\lambda_{1,K}$, $\lambda_{2,K}$ and $\lambda_{3,K}$ measure the amplitude of stretching. We now introduce c_τ the continuous, piecewise linear approximation in time defined by

$$c_\tau(x, t) = \frac{t - t^{n-1}}{\tau} c^n(x) + \frac{t^n - t}{\tau} c^{n-1}(x)$$

$$t^{n-1} \leq t \leq t^n, \quad x \in \Omega,$$

where c^{n-1} , c^n are computed using (6). Our simplified error indicator is then defined on each time

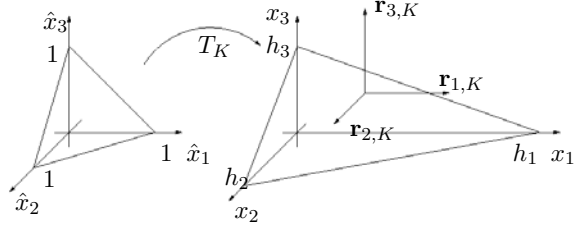


Figure 2: A simple example of transformation from the reference tetrahedron \hat{K} to the generic tetrahedron K .

interval $[t^{n-1}, t^n]$ and each tetrahedron K by

$$\begin{aligned} \left(\eta_{n,K}(c_\tau) \right)^2 &= \\ & \int_{t^{n-1}}^{t^n} \frac{1}{2\sqrt{\lambda_{1,K}\lambda_{2,K}\lambda_{3,K}}} \left\| \left[\frac{\partial c_\tau}{\partial n} \right] \right\|_{L^2(\partial K)} \\ & \times \left(\lambda_{1,K}^2 \left(\mathbf{r}_{1,K}^T G_K(c_\tau) \mathbf{r}_{1,K} \right) \right. \\ & \quad \left. + \lambda_{2,K}^2 \left(\mathbf{r}_{2,K}^T G_K(c_\tau) \mathbf{r}_{2,K} \right) \right. \\ & \quad \left. + \lambda_{3,K}^2 \left(\mathbf{r}_{3,K}^T G_K(c_\tau) \mathbf{r}_{3,K} \right) \right)^{1/2}. \quad (7) \end{aligned}$$

Here $G_K(c_\tau)$ is the 3×3 matrix defined by

$$(G_K(c_\tau))_{ij} = \int_K \eta_i^{ZZ}(c_\tau) \eta_j^{ZZ}(c_\tau) dx,$$

with $\eta_i^{ZZ}(c_\tau)$, $i = 1, 2, 3$, being the components of the so-called Zienkiewicz-Zhu error estimator

$$\begin{pmatrix} \eta_1^{ZZ}(c_\tau) \\ \eta_2^{ZZ}(c_\tau) \\ \eta_3^{ZZ}(c_\tau) \end{pmatrix} = \begin{pmatrix} (I - \Pi) \left(\frac{\partial c_\tau}{\partial x_1} \right) \\ (I - \Pi) \left(\frac{\partial c_\tau}{\partial x_2} \right) \\ (I - \Pi) \left(\frac{\partial c_\tau}{\partial x_3} \right) \end{pmatrix}, \quad (8)$$

where $\Pi \frac{\partial c_\tau}{\partial x_1}$, $\Pi \frac{\partial c_\tau}{\partial x_2}$ and $\Pi \frac{\partial c_\tau}{\partial x_3}$ are an approximate $L^2(\Omega)$ projection onto a finite element space. From constant values of $\partial c_\tau / \partial x_i$, $i = 1, 2, 3$, on triangles, values at vertices P are build using the

formula

$$\begin{pmatrix} \Pi \left(\frac{\partial c_\tau}{\partial x_1} \right) (P) \\ \Pi \left(\frac{\partial c_\tau}{\partial x_2} \right) (P) \\ \Pi \left(\frac{\partial c_\tau}{\partial x_3} \right) (P) \end{pmatrix} = \frac{1}{\sum_{P \in K} |K|} \begin{pmatrix} \sum_{P \in K} |K| \left(\frac{\partial c_\tau}{\partial x_1} \right) |K| \\ \sum_{P \in K} |K| \left(\frac{\partial c_\tau}{\partial x_2} \right) |K| \\ \sum_{P \in K} |K| \left(\frac{\partial c_\tau}{\partial x_3} \right) |K| \end{pmatrix}.$$

The matrix $G_K(c_\tau)$ is an estimation of the gradient error in tetrahedron K , therefore the term $\mathbf{r}_{1,K}^T G_K(c_\tau) \mathbf{r}_{1,K}$ in (7) contributes to measuring the error in the direction of the tetrahedron's maximum stretching and the term

$$\begin{aligned} & \int_{t^{n-1}}^{t^n} \frac{1}{2\sqrt{\lambda_{1,K}\lambda_{2,K}\lambda_{3,K}}} \left\| \left[\frac{\partial c_\tau}{\partial n} \right] \right\|_{L^2(\partial K)} \\ & \quad \times \lambda_{1,K} \left(\mathbf{r}_{1,K}^T G_K(c_\tau) \mathbf{r}_{1,K} \right)^{1/2} \end{aligned}$$

is nothing but the estimated error in the direction of the tetrahedron's maximum stretching.

The gradient error estimation can be justified theoretically whenever superconvergence occurs, that is when $\nabla c - \Pi \nabla c_\tau$ is better than $O(h)$. For an analysis of the behaviour and the convergence of the Zienkiewicz-Zhu error estimate in 3D see [Picasso (2006); Brandts and Křížek (2003)].

Our adaptive algorithm aims at building tetrahedral meshes with large aspect ratio such that the relative estimated error is close to a preset tolerance TOL , that is:

$$\begin{aligned} 0.75 TOL &\leq \frac{\left(\sum_{n=1}^N \sum_{\text{tetr. } K} \left(\eta_{n,K}(c_\tau) \right)^2 \right)^{1/2}}{\left(\int_0^T \int_\Omega |\nabla c_\tau|^2 \right)^{1/2}} \\ &\leq 1.25 TOL. \quad (9) \end{aligned}$$

A sufficient condition to satisfy (9) is to build, for each time interval (t_{n-1}, t_n) , $n = 1, \dots, N$, a tetrahedral mesh with large aspect ratio such that

$$\begin{aligned} \frac{0.75^2 TOL^2}{NV^n} \int_{t^{n-1}}^{t^n} \int_\Omega |\nabla c_\tau|^2 &\leq \left(\eta_{n,K}(c_\tau) \right)^2 \\ &\leq \frac{1.25^2 TOL^2}{NV^n} \int_{t^{n-1}}^{t^n} \int_\Omega |\nabla c_\tau|^2 \end{aligned}$$

for all tetrahedron K , where NV^n is the number of vertexes of the mesh at time t_n . We then proceed as in [Picasso (2003b,a)] to build a mesh having elements with high aspect ratio, using the MeshAdapt software [Distene (2003)] based on the mesh generator of the GAMMA research team of INRIA [Alauzet, George, Mohammadi, Frey, and Borouchaki (2003)]. A new metric is constructed as follows. For each tetrahedron, for each stretching direction $i = 1, 2, 3$, the mesh size in the i -th direction of stretching, $\lambda_{i,K}$, is updated in order to equidistribute the error indicator in the i -th direction of stretching

$$\int_{t^{n-1}}^{t^n} \frac{1}{2\sqrt{\lambda_{1,K}\lambda_{2,K}\lambda_{3,K}}} \left\| \left[\frac{\partial c_\tau}{\partial n} \right] \right\|_{L^2(\partial K)} \times \left(\lambda_{i,K}^2 \left(\mathbf{r}_{i,K}^T G_K(c_\tau) \mathbf{r}_{i,K} \right) \right)^{1/2}.$$

Then, the i -th direction of stretching $\mathbf{r}_{i,K}$ is aligned with the i -th eigenvector of the matrix $G_K(c_\tau)$. Then, the mesh adaptation software MeshAdapt is called to generate a new mesh.

4 Numerical results

Numerical results for simulations of dendritic growth of a single and several dendrites are presented in this section. All experiments were performed on a 1.6GHz AMD Opteron 64 bit workstation with 8Gb of RAM.

If not stated differently, the values of the parameters involved in (4), (3), (2) and (1) are reported in Table 1 and correspond to an Al-Cu alloy, see [Jacot and Rappaz (2002)], Table 1 column B. The temperature is $T = 993.8 K$, the time step is $\tau = 1 \times 10^{-4} s$, the interface width $\delta = 10^{-6} m$ and the penalty parameter $\varepsilon = 10^{-10}$.

Table 1: Values of the physical parameters.

T_m	1000 K	k	0.63
D_s	$5 \cdot 10^{-10} m^2/s$	D_l	$5 \cdot 10^{-9} m^2/s$
Γ	$5 \cdot 10^{-7} Km$	\bar{a}	0.04
μ_k	$0.0015 m/(Ks)$	m_l	-260 K
ρ_s	$1000 kg/m^3$	ρ_l	$950 kg/m^3$
μ_l	$0.014 kg/(ms)$		

4.1 Numerical validation

The first step is to validate the adaptive algorithm for the solidification problem in the simple test case. For this purpose we set the computational domain to $\Omega = [-0.00025, 0.00025]^3$. The densities in solid in liquid are equal so the fluid flow is absent. We add source terms in (3) and (4) so that ϕ and c are given by

$$\phi(r, t) = c(r, t) = \frac{1 - \tanh((r - r_0 - vt)/\delta)}{2} \quad (10)$$

where $r_0 = 0.00015 m$ is the initial size of a solid grain, $v = 0.001 m/s$ and $\delta = 10^{-5} m$. The final time is $t_{end} = 0.025 s$ and the time step $\tau = 2.5 \times 10^{-5} s$. Thus, c and ϕ varies smoothly across the diffused interface defined by a growing sphere. The mesh obtained after 100 time steps is shown in Figure 3.

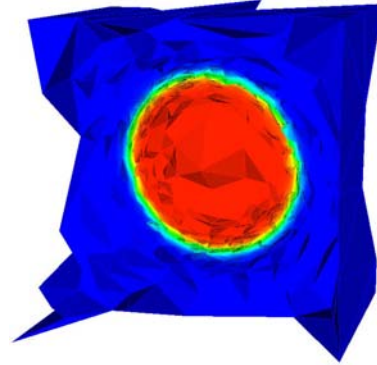


Figure 3: The numerical test case problem with known solution. The concentration field and anisotropic adapted mesh when $TOL = 0.25$.

The error

$$e = \left(\int_0^{t_{end}} \int_{\Omega} |\nabla(c - c_\tau)|^2 \right)^{1/2}$$

is reported in Table 2. Also, the effectivity indices (that is the ratio between the true and the estimated error) ei^{ZZ} and ei^A corresponding to Zienkiewicz-Zhu error estimator (8) and to our simplified error indicator (7), respectively, are shown. Numerical results confirm that the effectivity indices are mesh size and aspect ratio independent, as predicted in [Picasso (2006)] in the framework of the Laplace problem.

Table 2: Effectivity indices and numerical error when using the 3D adaptive algorithm with several values of TOL .

TOL	Vertices	e	ei^{ZZ}	ei^A
1	248	0.014	1.01	2.87
0.5	2397	0.0072	0.99	2.67
0.25	12161	0.0038	0.94	2.44
0.125	175482	0.0021	0.96	2.03
0.0625	1225084	0.0012	0.98	1.91

4.2 Single dendrite

We now present the solidification of a single dendrite. The initial solid grain is a circle of a diameter $5 \cdot 10^{-6} m$ of initial concentration the equilibrium liquid concentration of the phase diagram $k(T - T_m)/m_l$. The initial concentration in the liquid phase equals 0.02 and is between the liquidus concentration at equilibrium $(T - T_m)/m_l = 0.0238$ and the solidus concentration at equilibrium $k(T - T_m)/m_l = 0.015$. The domain is a cube of side $0.0005 m$. The results obtained for $TOL = 0.225$ are presented in Figures 4 and 7, the maximum observed velocity being $1 \cdot 10^{-5} m/s$ and the pressure drop $3 \cdot 10^{-6} Pa$.

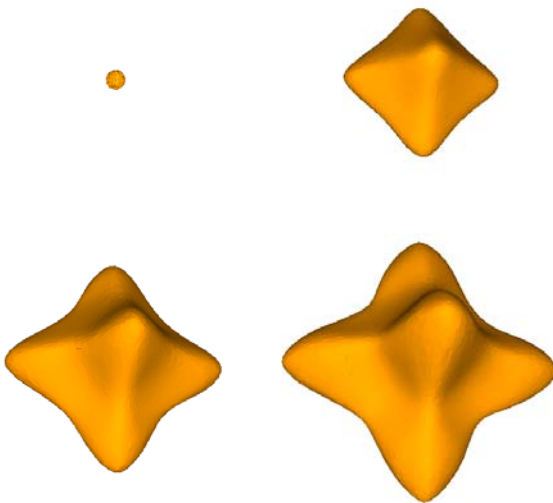


Figure 4: Single dendrite. Shape at times $t = 0, 0.25, 0.375$ and $0.5s$. The number of vertices is 10848, 31727, 46819 and 85476 respectively.

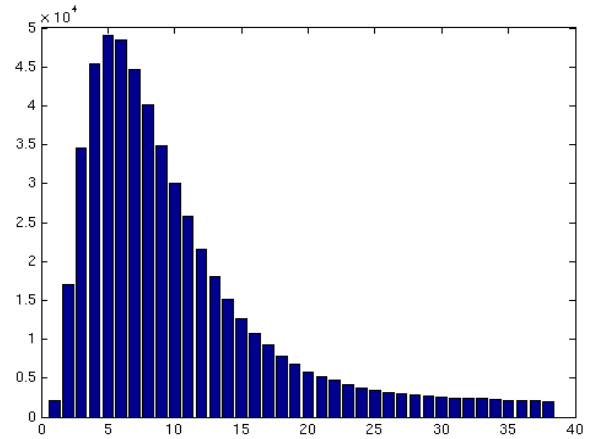


Figure 5: Single dendrite. Histogram of the mesh aspect ratio. The aspect ratio is on the horizontal axis and the number of tetrahedrons on the vertical axis.

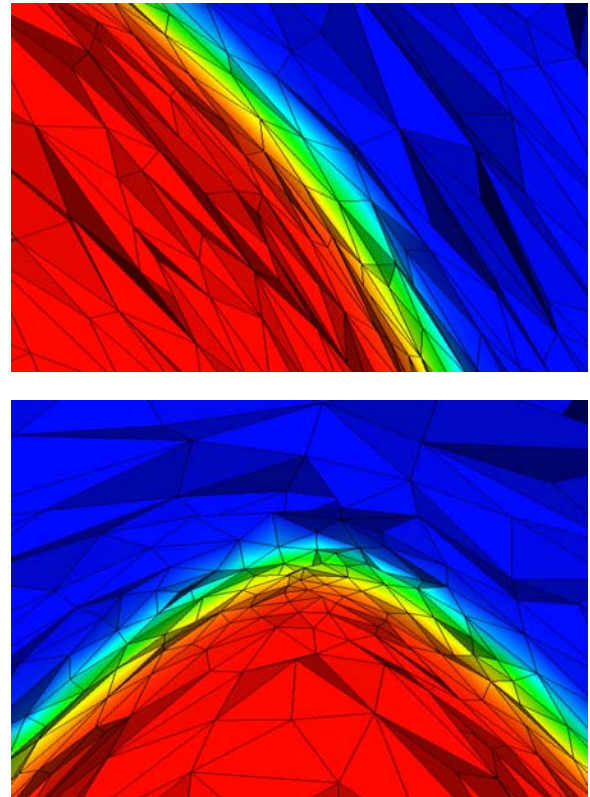


Figure 6: Single dendrite. Zoom of the phase field and adapted mesh along of a dendritic arm (top) and at a dendritic tip (bottom).

The CPU time was approximately two days. About 5000 time steps were used and the maximal number of vertices was 138487. The total number of remeshings was 210. The average aspect ratio $\lambda_{1,K}/\lambda_{3,K}$ was 78 for the final mesh, see Figure 5 for a histogram and Figure 6 for adapted meshes. The total amount of memory required by the simulation never exceeded 2Gb (the upper limit of memory that can be addressed on 32 bit computers), thus the simulations may be efficiently performed on the standard workstations.

It should be noted that the mesh adaptation software [Distene (2003)] was not always capable of generating the mesh respecting the metric calculated from our error indicator. In some cases the mesh was a lot finer than demanded, see for instance the last row of Figure 7.

4.3 Eight dendrites growing simultaneously

The liquid flow due to shrinkage is now computed around 8 dendrites. We place $2 \times 2 \times 2 = 8$ dendritic seeds in the computational domain Ω and let the system evolve observing the liquid flow and the pressure drop during the process. The distance between the seeds is $0.0002 m$, the size of the computational domain is $0.0006 m$. The results for $TOL = 0.225$ are presented in Figures 8 and 9.

The solidification shrinkage causes the liquid to flow toward the center of the cube. When the dendrites are sufficiently big, one can observe negative pressure appearing in the almost closed central region of the computational domain Ω . The maximum observed velocity being $1 \cdot 10^{-5} m/s$, as in the single dendrite case. The pressure drop is $6.5 \cdot 10^{-6} Pa$.

During the 2500 time steps 210 meshes were constructed. The average aspect ratio, was always close to 10 taking the value of 11.51 for the final mesh (see Figure 10 for a histogram). The simulation required at most 256263 mesh points and took approximately one week.

4.4 Comparison with the two dimensional simulations

Comparing numerical results for a single dendritic growth with the two dimensional simulations for the same physical parameters leads to the same observation as in [Jeong, Goldenfeld, and Dantzig (2001)] : the growth rate in three space dimensions is approximately two times bigger than in two space dimensions.

Comparison of multidendritic cases, eight dendrites in three dimensions with four dendrites in two dimensions is shown in the Table 3.

Table 3: Maximum velocity and pressure drop in 2D and 3D.

No. of dendrites	Max. velocity	pressure drop
2D - 4	$3.8 \cdot 10^{-6} m/s$	$8.7 \cdot 10^{-2} Pa$
3D - 8	$10 \cdot 10^{-6} m/s$	$6.5 \cdot 10^{-6} Pa$

Numerical results obtained for three dimensional simulations and those obtained in two dimensional differ significantly. In two dimensions a relatively large pressure drop in the region between the growing dendrites and a fast liquid flow between dendritic tips is observed. In three dimension while pressure drop and flow between dendritic tips is still observed it is much smaller than in 2D and the maximal values do not differ much from those obtained in the single dendrite simulations. This points out the fundamental differences between two and three dimensions.

Large pressure drop in the multidendritic simulations can be obtained much easier in two dimensional simulations — the liquid feeding the region between solidifying dendrites can flow only between dendritic tips. The small distance between the neighbouring dendritic tips means that the fluid velocity in that region should be relatively large in order to compensate the solidification shrinkage in the central part of the domain. The flow is generated by a large pressure drop. In three dimensions however even in the case of coalescence when the neighbouring dendrites con-

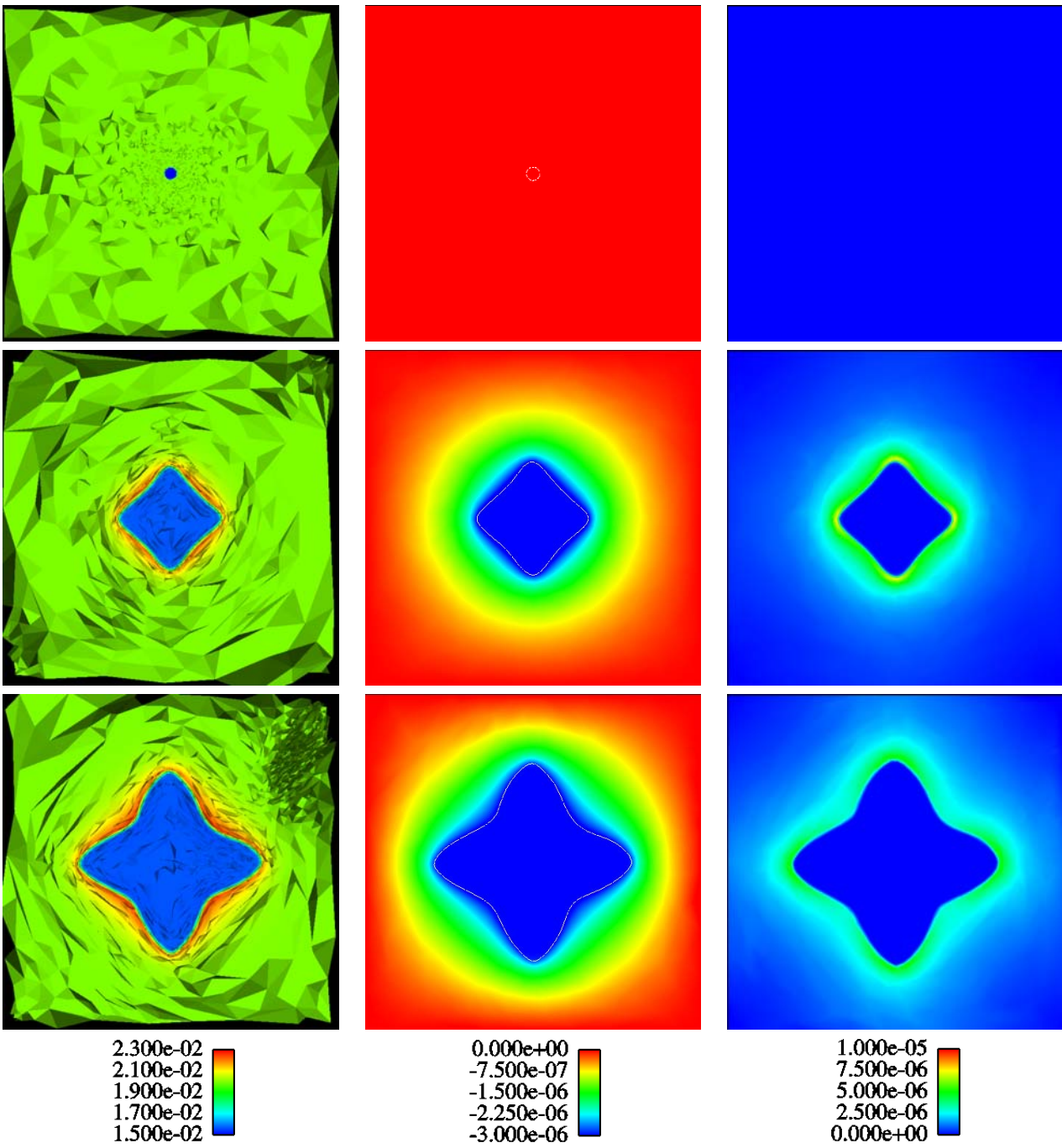


Figure 7: Single dendrite. Concentration field and adapted meshes (left column), pressure drop (middle column) and velocity field (right column) at times $t = 0, 0.25$ and 0.5 s.

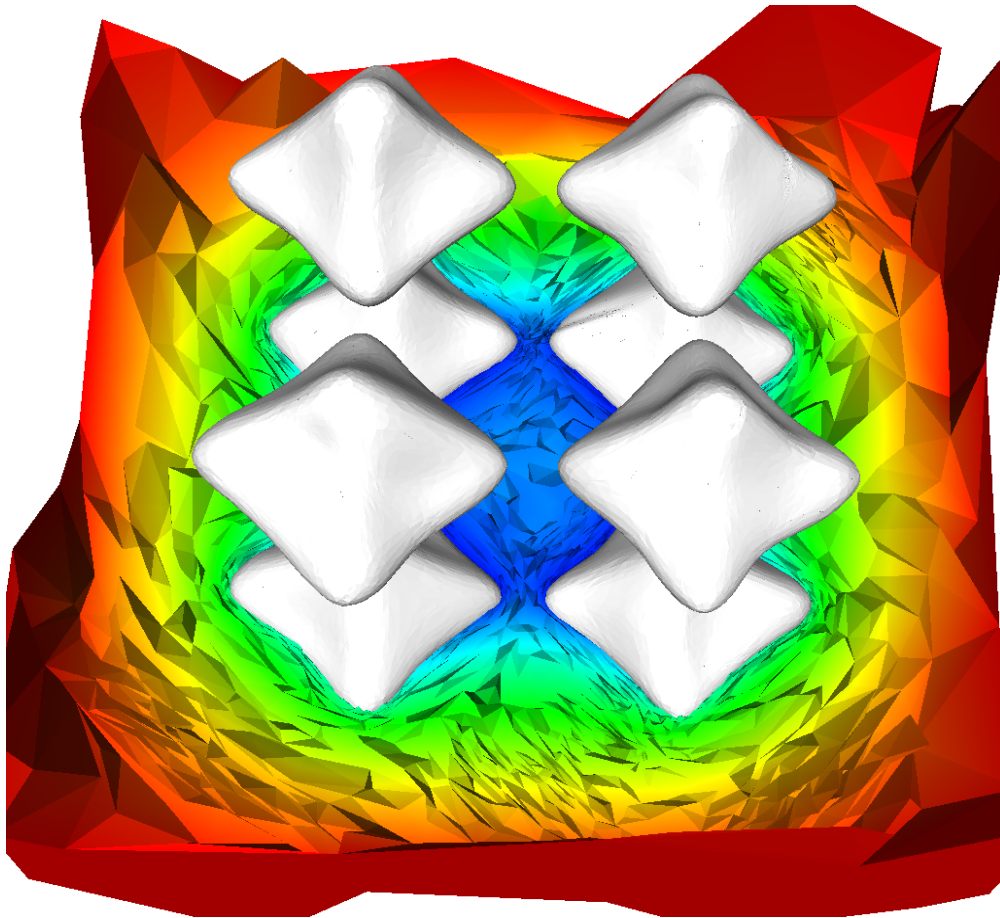


Figure 8: Eight dendrites. The pressure field and the adapted mesh at the crosssection containing the centers of four dendrites are shown.

nect with each other the fluid can still flow between the dendritic arms — contrary to 2D case, where the closed liquid region is created. A large pressure drop sufficient enough to trigger a microporosity formation in three dimensions is expected to appear in more complicated simulations. From the numerical point of view, 3D simulations are much more demanding than 2D simulations. Firstly, with the mesh generator we have used, it is currently impossible to obtain meshes with an aspect ratio as large as in 2D (up to 10000 in 2D, only 100 in 3D). In 3D (resp. 2D), since the number of vertices is proportional to TOL^{-3} (resp. TOL^{-2}), increasing the accuracy of the solution by a factor two yields $2^3 = 8$ (resp. $2^2 = 4$) times more unknowns. In this paper we have performed the simulation of 8 dendrites growing simultaneously until contact between the dendrites

tips, thus obtaining 256263 vertices. In [Narski and Picasso (2006)], the 2D simulation of 16 dendrites has been performed with two times less vertices.

However, the gain between isotropic and anisotropic meshes more favorable in 3D than in 2D. Indeed, in 3D, using a mesh with aspect ratio 5-5-1 (that is to say elements with mesh size 5 times larger in two directions than in the third one), requires $5^2 = 25$ times less vertices than an isotropic mesh with aspect ratio 1-1-1. On the other side, in 2D, using a mesh with aspect ratio 5-1, requires 5 times less vertices than an isotropic mesh with aspect ratio 1-1.

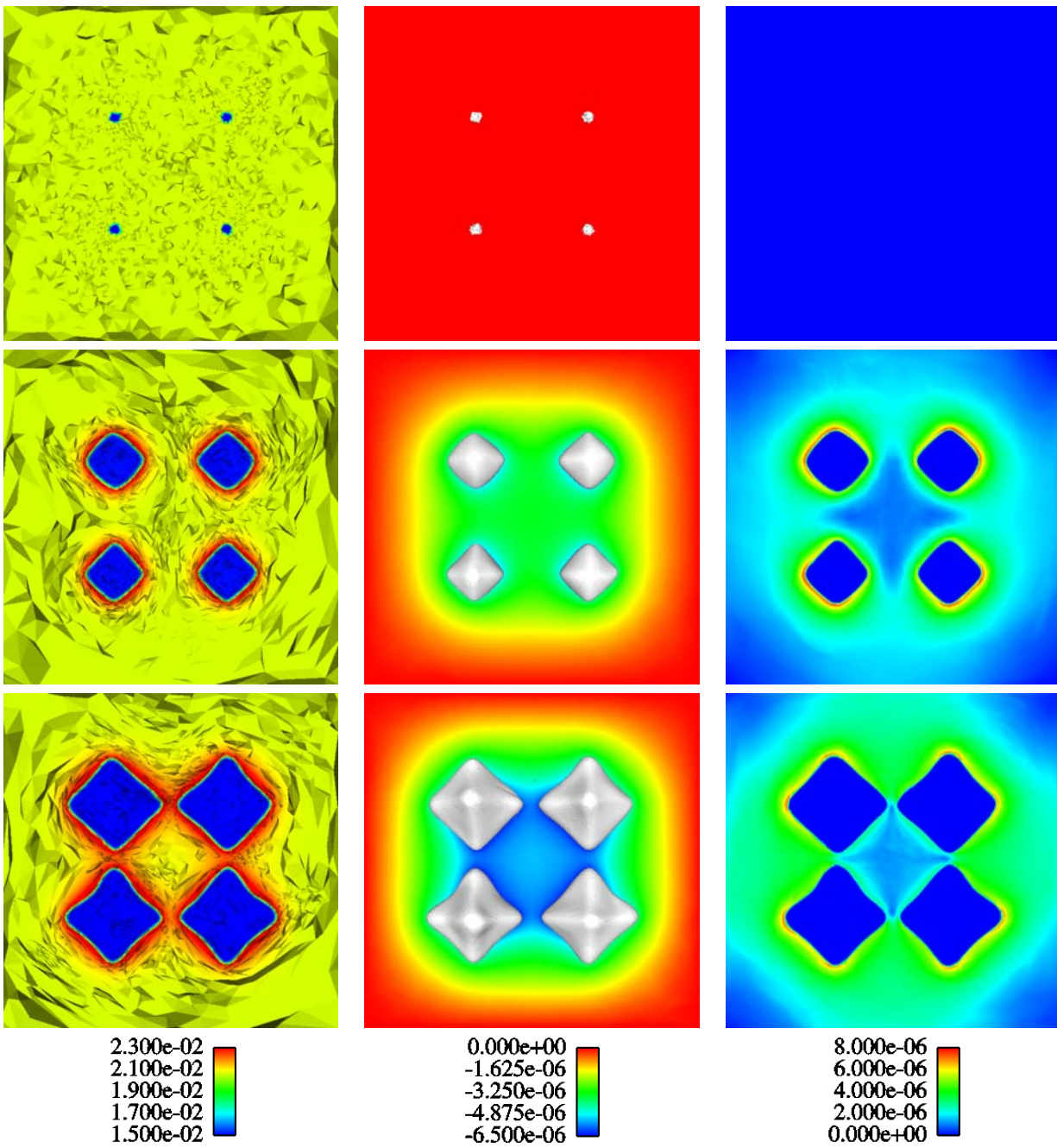


Figure 9: Eight dendrites. Concentration field and adapted meshes (left column), pressure drop (middle column) and velocity field (right column) at times $t = 0, 0.25$ and $0.5s$. The results represent the fields on the crosssection passing through four dendritic centers.

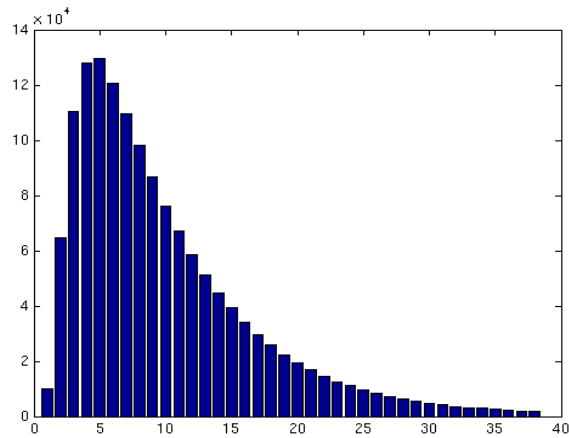


Figure 10: Eight dendrites. Histogram of the mesh aspect ratio.

5 Conclusions

We presented an efficient adaptive algorithm for simulating the dendritic growth with convection. The anisotropic finite elements allows to construct meshes with less than 300000 vertices even for simulations involving several dendrites growing simultaneously.

The splitting scheme applied to the fluid flow equations drastically reduces the memory requirements and allows complicated 3D simulations to be performed on a standard workstation. We have studied the effects of the liquid flow induced by the solidification shrinkage. The pressure drop due to solutal contraction appearing between solidifying dendrites can be obtained. However, this pressure drop is not sufficient in order to explain the formation of gas bubbles observed during microporosity.

Acknowledgement: The authors wish to thank Michel Rappaz and Alain Jacot from the Institute of Materials, EPFL, for many helpful discussion concerning the physics of solidification. Virabouth Prachittham is acknowledged for implementation.

References

Alauzet, F.; George, P. L.; Mohammadi, B.; Frey, P.; Borouchaki, H. (2003): Transient fixed

point-based unstructured mesh adaptation. *Internat. J. Numer. Methods Fluids*, vol. 43, no. 6-7, pp. 729–745. ECCOMAS Computational Fluid Dynamics Conference, Part II (Swansea, 2001).

Anderson, D. M.; McFadden, G. B.; Wheeler, A. A. (2000): A phase-field model of solidification with convection. *Phys. D*, vol. 135, no. 1-2, pp. 175–194.

Anderson, D. M.; McFadden, G. B.; Wheeler, A. A. (2001): A phase-field model with convection: sharp-interface asymptotics. *Phys. D*, vol. 151, no. 2-4, pp. 305–331.

Beckermann, C.; Diepers, H.; Steinbach, I.; Karma, A.; Tong, X. (1999): Modeling melt convection in phase-field simulations of solidification. *J. Comput. Phys.*, vol. 154, no. 2, pp. 468–496.

Boettinger, W.; Coriell, S.; Greer, A.; Karma, A.; Kurz, W.; Rappaz, M.; Trivedi, R. (2000): Solidification microstructures: Recent developments, future directions. *Acta Materialia*, vol. 48, no. 1, pp. 43–70.

Boettinger, W.; Warren, J.; Beckermann, C.; Karma, A. (2002): Phase-field simulation of solidification. *Annu. Rev. Mater. Res.*, vol. 32, pp. 163–194.

Brandts, J.; Křížek, M. (2003): Gradient superconvergence on uniform simplicial partitions of polytopes. *IMA J. Numer. Anal.*, vol. 23, no. 3, pp. 489–505.

Burman, E.; Jacot, A.; Picasso, M. (2004): Adaptive finite elements with high aspect ratio for the computation of coalescence using a phase-field model. *J. Comput. Phys.*, vol. 195, no. 1, pp. 153–174.

Burman, E.; Picasso, M. (2003): Anisotropic, adaptive finite elements for the computation of a solutal dendrite. *Interfaces Free Bound.*, vol. 5, no. 2, pp. 103–127.

Burman, E.; Rappaz, J. (2003): Existence of solutions to an anisotropic phase-field model. *Math. Methods Appl. Sci.*, vol. 26, no. 13, pp. 1137–1160.

- Caginalp, G.; Xie, W.** (1993): Phase-field and sharp-interface alloy models. *Phys. Rev. E* (3), vol. 48, no. 3, pp. 1897–1909.
- Chen, L.** (2002): Phase-field models for microstructure evolutions. *Annual Rev. Mater. Res.*, vol. 32, pp. 163–194.
- Collins, J.; Levine, H.** (1985): Diffuse interface model of diffusion-limited crystal growth. *Phys. Rev. B*, vol. 31, no. 9, pp. 6119–6122.
- Conti, M.** (2001): Density change effects on crystal growth from the melt. *Phys. Rev. E*, vol. 64, no. 5, pp. 051601.
- Conti, M.** (2004): Advection flow effects in the growth of a free dendrite. *Physical Review E (Statistical, Nonlinear, and Soft Matter Physics)*, vol. 69, no. 2, pp. 022601.
- Creusé, E.; Nicaise, S.** (2006): Anisotropic a posteriori error estimation for the mixed discontinuous Galerkin approximation of the Stokes problem. *Numer. Methods Partial Differential Equations*, vol. 22, no. 2, pp. 449–483.
- Distene** (2003): *MeshAdapt : A mesh adaptation tool, User's manual Version 3.0*. Distene S.A.S., Pôle Teratec - BARD-1, Domaine du Grand Rué, 91680 Bruyères-le-Chatel, France, 2003.
- Echebarria, B.; Folch, R.; Karma, A.; Plapp, M.** (2004): Quantitative phase-field model of alloy solidification. *Phys. Rev. E*, vol. 70, no. 6, pp. 061604.
- Formaggia, L.; Micheletti, S.; Perotto, S.** (2004): Anisotropic mesh adaptation in computational fluid dynamics: application to the advection-diffusion-reaction and the Stokes problems. *Appl. Numer. Math.*, vol. 51, no. 4, pp. 511–533.
- Formaggia, L.; Perotto, S.** (2001): New anisotropic a priori error estimates. *Numer. Math.*, vol. 89, no. 4, pp. 641–667.
- Formaggia, L.; Perotto, S.** (2003): Anisotropic error estimates for elliptic problems. *Numer. Math.*, vol. 94, pp. 67–92.
- Fried, M.** (2004): A level set based finite element algorithm for the simulation of dendritic growth. *Comput. Vis. Sci.*, vol. 7, no. 2, pp. 97–110.
- Gibou, F.; Fedkiw, R.; Caffisch, R.; Osher, S.** (2003): A level set approach for the numerical simulation of dendritic growth. *J. Sci. Comput.*, vol. 19, no. 1-3, pp. 183–199.
- Griebel, M.; Merz, W.; Neunhoffer, T.** (1999): Mathematical modeling and numerical simulation of freezing processes of a supercooled melt under consideration of density changes. *Comp. Vis. Sci.*, vol. 1, no. 4, pp. 201–219.
- Heinrich, J. C.; Poirier, D. R.** (2004): Convection modeling in directional solidification. *C. R. Mecanique*, vol. 332, pp. 429–445.
- Hong, C. P.; Zhu, M. F.; Lee, S. Y.** (2006): Modeling of dendritic growth in alloy solidification with melt convection. *FDMP: Fluid Dynamics & Materials Processing*, vol. 2, no. 4, pp. 247–260.
- Jacot, A.; Rappaz, M.** (2002): A pseudo-front tracking technique for the modelling of solidification microstructures in multi-component alloys. *Acta Mater.*, vol. 50, no. 8, pp. 1909–1926.
- Jeong, J.; Goldenfeld, N.; Dantzig, J.** (2001): Phase field model for three-dimensional dendritic growth with fluid flow. *Phys. Rev. E*, vol. 64, no. 4, pp. 041602.
- Juric, D.; Tryggvason, G.** (1996): A front-tracking method for dendritic solidification. *J. Comput. Phys.*, vol. 123, no. 1, pp. 127–148.
- Karma, A.** (1994): Phase-field model of eutectic growth. *Phys. Rev. E*, vol. 49, pp. 2245–2250.
- Kobayashi, R.** (1993): Modeling and numerical simulations of dendritic crystal growth. *Physica D*, vol. 63, pp. 410–423.
- Kunert, G.** (2000): An a posteriori residual error estimator for the finite element method on anisotropic tetrahedral meshes. *Numer. Math.*, vol. 86, no. 3, pp. 471–490.

- Micheletti, S.; Perotto, S.; Picasso, M.** (2003): Stabilized finite elements on anisotropic meshes: a priori error estimates for the advection-diffusion and the Stokes problems. *SIAM J. Numer. Anal.*, vol. 41, no. 3, pp. 1131–1162 (electronic).
- Narski, J.; Picasso, M.** (2006): Adaptive finite elements with high aspect ratio for dendritic growth of a binary alloy including fluid flow induced by shrinkage. *submitted to Computer Methods in Applied Mechanics and Engineering*.
- Nestler, B.; Wheeler, A. A.; Ratke, L.; Stöcker, C.** (2000): Phase-field model for solidification of a monotectic alloy with convection. *Phys. D*, vol. 141, no. 1-2, pp. 133–154.
- Ni, J.; Beckermann, C.** (1991): A volume-averaged 2-phase model for transport phenomena during solidification. *Metall. Trans. B*, vol. 22, no. 3, pp. 349–361.
- Picasso, M.** (2003): An anisotropic error indicator based on Zienkiewicz-Zhu error estimator: application to elliptic and parabolic problems. *SIAM J. Sci. Comput.*, vol. 24, no. 4, pp. 1328–1355 (electronic).
- Picasso, M.** (2003): Numerical study of the effectivity index for an anisotropic error indicator based on Zienkiewicz-Zhu error estimator. *Comm. Numer. Methods Engrg.*, vol. 19, no. 1, pp. 13–23.
- Picasso, M.** (2005): An adaptive algorithm for the Stokes problem using continuous, piecewise linear stabilized finite elements and meshes with high aspect ratio. *Appl. Numer. Math.*, vol. 54, no. 3-4, pp. 470–490.
- Picasso, M.** (2005): An adaptive algorithm for the Stokes problem using continuous, piecewise linear stabilized finite elements and meshes with high aspect ratio. *Appl. Numer. Math.*, vol. 54, no. 3-4, pp. 470–490.
- Picasso, M.** (2006): Adaptive finite elements with large aspect ratio based on an anisotropic error estimator involving first order derivatives. *Comput. Methods Appl. Mech. Engrg.*, vol. 196, no. 1-3, pp. 14–23.
- Picasso, M.; Rappaz, J.** (2001): Stability of time-splitting schemes for the Stokes problem with stabilized finite elements. *Numer. Methods Partial Differential Equations*, vol. 17, no. 6, pp. 632–656.
- Provatas, N.; Goldenfeld, N.; Dantzig, J.** (1999): Adaptive mesh refinement computation of solidification microstructures using dynamic data structures. *J. Comput. Phys.*, vol. 148, no. 1, pp. 265–290.
- Randrianarivony, M.** (2004): Anisotropic finite elements for the Stokes problem: a posteriori error estimator and adaptive mesh. *J. Comput. Appl. Math.*, vol. 169, no. 2, pp. 255–275.
- Schmidt, A.** (1996): Computation of three dimensional dendrites with finite elements. *J. Comput. Phys.*, vol. 125, no. 2, pp. 293–312.
- Sun, Y.; Beckermann, C.** (2004): Diffuse interface modeling of two-phase flows based on averaging: mass and momentum equations. *Phys. D*, vol. 198, no. 3-4, pp. 281–308.
- Tönhardt, R.; Amberg, G.** (2000): Simulation of natural convection effects on succinonitrile crystals. *Phys. Rev. E*, vol. 62, pp. 828.
- Warren, J.; Boettinger, W.** (1995): Prediction of dendritic growth and microsegregation patterns in a binary alloy using the phase-field model. *Acta Metall. Mater.*, vol. 43, no. 2, pp. 689–703.